







RESEARCH ARTICLE | APRIL 13 2023

## Diffusion of Sn donors in $\beta\text{-Ga}_2\text{O}_3$

Ymir K. Frodason ; Patryk P. Krzyzaniak ; Lasse Vines ; Joel B. Varley ; Chris G. Van de Walle ; Klaus Magnus H. Johansen 



APL Mater. 11, 041121 (2023)

<https://doi.org/10.1063/5.0142671>



CrossMark

### AIP Advances

Why Publish With Us?

-  **25 DAYS**  
average time to 1st decision
-  **740+ DOWNLOADS**  
average per article
-  **INCLUSIVE**  
scope

[Learn More](#)



# Diffusion of Sn donors in $\beta$ -Ga<sub>2</sub>O<sub>3</sub>

Cite as: APL Mater. 11, 041121 (2023); doi: 10.1063/5.0142671

Submitted: 16 January 2023 • Accepted: 31 March 2023 •

Published Online: 13 April 2023



View Online



Export Citation



CrossMark

Ymir K. Frodason,<sup>1,a)</sup> Patryk P. Krzyzaniak,<sup>1</sup> Lasse Vines,<sup>1</sup> Joel B. Varley,<sup>2</sup> Chris G. Van de Walle,<sup>3</sup>   
and Klaus Magnus H. Johansen<sup>1</sup>

## AFFILIATIONS

<sup>1</sup>Department of Physics, Centre for Materials Science and Nanotechnology, University of Oslo, N-0318 Oslo, Norway

<sup>2</sup>Lawrence Livermore National Laboratory, Livermore, California 94550, USA

<sup>3</sup>Materials Department, University of California, Santa Barbara, California 93106-5050, USA

<sup>a)</sup>Author to whom correspondence should be addressed: ymirkf@fys.uio.no

## ABSTRACT

Diffusion of the *n*-type dopant Sn in  $\beta$ -Ga<sub>2</sub>O<sub>3</sub> is studied using secondary-ion mass spectrometry combined with hybrid functional calculations. The diffusion of Sn from a Sn-doped bulk substrate with surface orientation (001) into an epitaxial layer is observed after heat treatments in the temperature range of 1050–1250 °C. Calculated formation energies of Sn-related and intrinsic defects show that the migration of Sn is mediated by Ga vacancies ( $V_{\text{Ga}}$ ) through the formation and dissociation of intermittent mobile  $V_{\text{Ga}}\text{Sn}_{\text{Ga}}$  complexes. The evolution of the Sn concentration vs depth profiles after heat treatments can be well described by a reaction–diffusion model. Using model parameters guided by the hybrid functional calculations, we extract a  $V_{\text{Ga}}\text{Sn}_{\text{Ga}}$  complex migration barrier of  $3.0 \pm 0.4$  eV with a diffusion coefficient of  $2 \times 10^{-1}$  cm<sup>2</sup>/s. The extracted migration barrier is consistent with our theoretical predictions using the nudged elastic band method, which shows migration barriers of 3.42, 3.15, and 3.37 eV for the [100], [010], and [001] directions, respectively.

© 2023 Author(s). All article content, except where otherwise noted, is licensed under a Creative Commons Attribution (CC BY) license (<http://creativecommons.org/licenses/by/4.0/>). <https://doi.org/10.1063/5.0142671>

## I. INTRODUCTION

Monoclinic gallium sesquioxide ( $\beta$ -Ga<sub>2</sub>O<sub>3</sub>) has become a focus of much attention as a semiconductor with high potential for applications in power electronics. The main advantage is the unique combination of an ultra-wide bandgap of  $\sim 4.9$  eV<sup>1</sup>—leading to a high breakdown electric field—and control of the charge carrier concentration over a wide range from  $\sim 10^{14}$  to  $10^{20}$  cm<sup>-3</sup>.<sup>2</sup> This, in conjunction with the availability of melt-grown single-crystals and high-quality epitaxial layers,<sup>3,4</sup> has led to rapid development of high-voltage field-effect transistors<sup>5,6</sup> and Schottky barrier diodes.<sup>7</sup> Essential to this development is the precise control of dopant distributions, which relies on a solid understanding of the dopant diffusion process. Moreover, since dopant diffusion is almost invariably assisted by native point defects,<sup>8</sup> understanding dopant diffusion can also yield insight into the interplay between dopants and defects.

Sn substituting on a Ga site ( $\text{Sn}_{\text{Ga}}$ ) acts as a shallow single donor and is one of the most commonly utilized *n*-type dopants in  $\beta$ -Ga<sub>2</sub>O<sub>3</sub>.<sup>9–13</sup> Previous experimental studies on Sn diffusion have focused on Sn introduced by ion implantation and subjected to

rapid thermal annealing,<sup>14–16</sup> which is a convenient method for doping.<sup>17,18</sup> Recently, Tadjer *et al.*<sup>14</sup> and Sharma *et al.*<sup>15</sup> reported Sn diffusivities of  $1.68 \times 10^{-13}$  cm<sup>2</sup>/s at 1150 °C and  $2.7 \times 10^{-13}$  cm<sup>2</sup>/s at 1100 °C, respectively, in Sn-implanted bulk (–201)  $\beta$ -Ga<sub>2</sub>O<sub>3</sub>. A strong dependence on annealing ambient was noted, where diffusion was observed in O<sub>2</sub> and suppressed in N<sub>2</sub>.<sup>15</sup> In addition to Sn, Sharma *et al.*<sup>15,19</sup> explored the diffusion of Si and Ge implanted into bulk (–201)  $\beta$ -Ga<sub>2</sub>O<sub>3</sub> and found the diffusivity of Ge ( $1.1 \times 10^{-11}$  cm<sup>2</sup>/s at 1100 °C) to be significantly higher compared to Sn and Si ( $4.5 \times 10^{-12}$  cm<sup>2</sup>/s at 1100 °C). We note, however, that ion implantation generates defects, which can, e.g., lead to transient enhanced diffusion, making it more challenging to model the dopant diffusion and interpret extracted diffusion parameters.

Diffusion studies in  $\beta$ -Ga<sub>2</sub>O<sub>3</sub> are also complicated by the low symmetry of the monoclinic crystal structure. This can lead to strong anisotropy in diffusion parameters,<sup>20</sup> a plethora of crystallographically inequivalent defect configurations,<sup>21</sup> and intricate atomistic migration pathways.<sup>21,22</sup> In view of this, first-principles calculations for defects have been particularly valuable. For example, such calculations revealed three split Ga vacancy configurations, namely,  $V_{\text{Ga}}^{\text{ia}}$ ,

$V_{\text{Ga}}^{\text{ib}}$  and  $V_{\text{Ga}}^{\text{ic}}$ , where the latter two were found to be energetically preferred over the simple Ga vacancy on the Ga1 ( $V_{\text{Ga}1}$ ) or Ga2 site ( $V_{\text{Ga}2}$ ).<sup>22–25</sup> Peelaers *et al.*<sup>26</sup> have explored the diffusion mechanisms for Mg and N acceptor impurities based on defect formation energies and migration barriers obtained from hybrid functional calculations. Varley *et al.*<sup>9</sup> reported formation energies of  $\text{Sn}_{\text{Ga}}$ , but first-principles studies on Sn diffusion are not available.

In this work, Sn is diffused from an intentionally Sn-doped bulk substrate into an epitaxial thin film. Secondary-ion mass spectrometry (SIMS) is used to measure Sn concentration–depth profiles after sequential heat treatments. The profiles are analyzed using a reaction–diffusion (RD) model with parameters guided by formation energies and migration barriers obtained from first-principles calculations to obtain a consistent numerical solution to the diffusion equations. Migration of Sn is found to be mediated by Ga vacancies ( $V_{\text{Ga}}$ ) through the formation of mobile  $V_{\text{Ga}}\text{Sn}_{\text{Ga}}$  complexes, and the diffusivity of these complexes is extracted from the RD modeling. Migration barriers for  $V_{\text{Ga}}\text{Sn}_{\text{Ga}}$  are also calculated using the nudged elastic band (NEB) method,<sup>27</sup> elucidating the migration pathways and lattice anisotropy.

## II. METHODOLOGY

### A. Experimental details

The  $\beta\text{-Ga}_2\text{O}_3$  wafer used in this study was purchased from *Novel Crystal Technology Inc.* and consisted of a  $\sim 4.7\ \mu\text{m}$  thick thin film grown by halide vapor-phase epitaxy on a Sn-doped bulk substrate with (001) surface orientation. To realize diffusion of Sn from the substrate into the epilayer, a sample was sequentially heat treated for 30 min under pure  $\text{O}_2$  gas flow from 1000 to 1250 °C in steps of 50 °C.

A Cameca IMS7f SIMS utilizing a 10 keV  $\text{O}_2^+$  primary ion beam source was used to measure the concentration vs depth profiles of Sn, Si, and Fe in the samples. Absolute Sn, Si, and Fe concentration values were obtained by measuring ion-implanted reference samples. Depth calibration was performed by measuring the sputtered crater depth using a Dektak 8 stylus profilometer and assuming a constant erosion rate.

### B. Computational details

#### 1. Diffusion modeling

The differential equations used to simulate the measured Sn diffusion profiles were numerically solved using the FLEXPDE software.<sup>28</sup> Profiles were modeled sequentially, i.e., SIMS data from one temperature step were used as input for the subsequent one. Fitting parameters were manually adjusted to minimize the difference between the simulated and experimental data. The differential equations, input parameters, boundary conditions, and fitting parameters are presented in Sec. III D.

#### 2. First-principles defect calculations

To gain insight into the formation and migration of Sn-related and intrinsic defects in  $\beta\text{-Ga}_2\text{O}_3$ , first-principles calculations based on the generalized Kohn–Sham theory were performed. We used the projector augmented wave method<sup>29,30</sup> and

the Heyd–Scuseria–Ernzerhof (HSE)<sup>31</sup> screened hybrid functional, as implemented in the VASP code.<sup>32</sup> Semicore Ga and Sn  $3d$  electrons were included explicitly as valence electrons, and the fraction of screened Hartree–Fock exchange was adjusted to 33%, resulting in an accurate description of the experimental bandgap (4.9 eV direct bandgap) and lattice parameters ( $a = 12.23\ \text{\AA}$ ,  $b = 3.03\ \text{\AA}$ ,  $c = 5.79\ \text{\AA}$ , and  $\beta = 103.8^\circ$ ).

For defect calculations, we employed 160-atom supercells, a plane-wave cutoff of 400 eV and a single special  $k$ -point at (0.25, 0.25, 0.25). Defect formation energies and thermodynamic charge–state transition levels were evaluated using the formalism described in Ref. 33. For example, the formation energy of  $V_{\text{Ga}}^q$  is given by

$$E^f(V_{\text{Ga}}^q) = E_{\text{tot}}(V_{\text{Ga}}^q) - E_{\text{tot}}(\text{Ga}_2\text{O}_3) + \mu_{\text{Ga}} + qE_{\text{F}} + \Delta^q, \quad (1)$$

where  $E_{\text{tot}}[V_{\text{Ga}}^q]$  and  $E_{\text{tot}}[\text{Ga}_2\text{O}_3]$  are the total energies of the supercell containing the Ga vacancy in charge state  $q$  and perfect crystal, respectively. The removed Ga is placed in a reservoir with chemical potential  $\mu_{\text{Ga}}$ , and electrons are exchanged with the Fermi level  $E_{\text{F}}$ , which is referenced to the valence-band maximum (VBM). The chemical potential is varied between the Ga- and O-rich limits. Under Ga-rich conditions,  $\mu_{\text{Ga}}$  is given by the calculated energy per atom in pure Ga ( $\mu_{\text{Ga}}^0$ ). In the O-rich limit,  $\mu_{\text{Ga}}$  is bounded by the thermodynamic stability condition of  $\beta\text{-Ga}_2\text{O}_3$ , i.e.,  $\mu_{\text{Ga}} = \mu_{\text{Ga}}^0 + \frac{1}{2}\Delta H_{\text{f}}(\beta\text{-Ga}_2\text{O}_3)$ , where  $\Delta H_{\text{f}}(\beta\text{-Ga}_2\text{O}_3) = -10.22\ \text{eV}$  is the calculated heat of formation of  $\beta\text{-Ga}_2\text{O}_3$ . The chemical potential of Sn impurities is similarly bounded by the stability of the solubility-limiting phase  $\text{SnO}_2$ . Finally, the term  $\Delta^q$  is a finite-size correction for charged defects, calculated here by following the scheme outlined in Ref. 34 and 35.

Defect migration barriers were calculated using the NEB method<sup>27</sup> with at least five images, converging the forces to within 30 meV/Å. Owing to the large number of migration barriers that had to be considered, and the high associated computational cost, these calculations were performed using the strongly constrained and appropriately normed (SCAN) semilocal functional.<sup>36</sup> The lattice parameters were kept fixed to those computed using HSE (these are anyway in close agreement with those obtained using SCAN:  $a = 12.25\ \text{\AA}$ ,  $b = 3.04\ \text{\AA}$ ,  $c = 5.82\ \text{\AA}$ , and  $\beta = 103.8^\circ$ ). NEB calculations at the HSE level were then performed for the rate-limiting step for defect migration in each crystal direction, starting from the geometries obtained from SCAN NEB calculations. Only HSE results are shown here. SCAN results and details of defect configurations and migration pathways are provided in the [supplementary material](#).<sup>37</sup>

## III. RESULTS AND DISCUSSION

Figure 1 shows the Sn concentration as a function of depth for the as-grown and isochronally heat-treated sample, as measured by SIMS. Prior to the heat treatments, the measured concentration of Sn in the substrate was  $1.4 \times 10^{18}\ \text{cm}^{-3}$ , followed by a sharp decrease in the concentration at the interface between the epilayer and substrate. Sn diffusion from the substrate into the epilayer is observed starting at a temperature of 1050 °C. All measured Sn diffusion profiles are characterized by a plateau and a steep drop in concentration at the diffusion front.

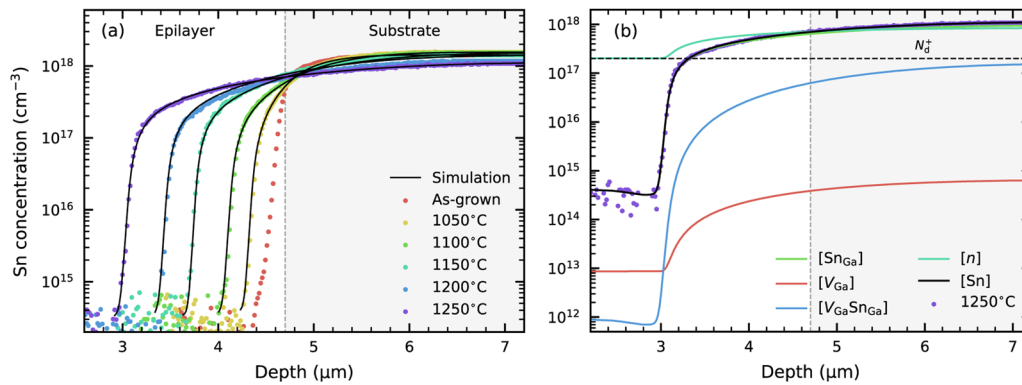


**FIG. 1.** (a) Sn concentration–depth profiles for the isochronally heat-treated sample (30 min from 1050 to 1250 °C), measured by SIMS (dots) and simulated using the RD model (black lines). The substrate and epilayer regions are indicated. (b) Depth distribution of  $\text{Sn}_{\text{Ga}}$ ,  $V_{\text{Ga}}$ ,  $V_{\text{Ga}}\text{Sn}_{\text{Ga}}$ , and  $n$  obtained from RD modeling of the 1250 °C Sn diffusion profile. The effective background-donor concentration  $N_{\text{d}}^{+}$  used in the modeling is indicated by the black dashed line. Concentrations of other defect species in (b) are determined via charge-neutrality considerations as described by Eqs. (6) and (7) and in the main text.

## A. Formation energies and diffusion mechanism

Two different diffusion mechanisms can be envisioned for  $\text{Sn}_{\text{Ga}}$ : (i) a vacancy mechanism, where  $\text{Sn}_{\text{Ga}}$  migrates by making a series of exchanges with  $V_{\text{Ga}}$ , which can also form complexes with  $\text{Sn}_{\text{Ga}}$ , or (ii) an interstitial–substitutional mechanism, which can occur by fast diffusion of interstitial Sn ( $\text{Sn}_{\text{i}}$ ) and subsequent changeover to  $\text{Sn}_{\text{Ga}}$ , mediated by  $\text{Ga}_{\text{i}}$  (kick-out mechanism:  $\text{Sn}_{\text{i}} \rightleftharpoons \text{Sn}_{\text{Ga}} + \text{Ga}_{\text{i}}$ ) or  $V_{\text{Ga}}$  (dissociative mechanism:  $\text{Sn}_{\text{Ga}} \rightleftharpoons \text{Sn}_{\text{i}} + V_{\text{Ga}}$ ). The activation energy for these mechanisms depends on the energy cost associated with the formation and migration of the impurity and diffusion-mediating intrinsic defects. Formation energies, in turn, depend on the Fermi-level position and chemical potentials.

Figure 2 shows formation energies obtained from hybrid functional calculations for the relevant point defects. In line with previous work,<sup>38</sup>  $\text{Sn}_{\text{Ga}}$  is a favorable shallow donor and strongly prefers the octahedral Ga2 site over the tetrahedral Ga1 site (1.06 eV difference in formation energy). Both  $\text{Sn}_{\text{i}}$  and  $\text{Ga}_{\text{i}}$  are highly unfavorable in  $n$ -type material and become relevant only for lower Fermi-level positions and under Ga-rich conditions. In contrast,  $V_{\text{Ga}}$  exhibits low formation energies under  $n$ -type conditions and is likely to be present as a compensating acceptor in Sn-doped material. Note that only the minimum formation energies over the different configurations of  $V_{\text{Ga}}$  and  $\text{Ga}_{\text{i}}$  are shown in Fig. 2 (denoted  $V_{\text{Ga}}^{\text{min}}$  and  $\text{Ga}_{\text{i}}^{\text{min}}$ ). Formation energies for all explored  $V_{\text{Ga}}$  and  $\text{Ga}_{\text{i}}$  configurations can be found in Refs. 25 and 39.

Considering Fermi-level positions in the upper part of the bandgap ( $\beta\text{-Ga}_2\text{O}_3$  is primarily  $n$ -type<sup>40</sup>), interstitial–substitutional mechanisms are unlikely to play a significant role for Sn diffusion, even though interstitial migration barriers are generally low.<sup>39,41</sup> Indeed, for the dissociative mechanism, the reaction  $\text{Sn}_{\text{Ga}} \rightarrow \text{Sn}_{\text{i}} + V_{\text{Ga}}$  is associated with an energy cost as high as 8.2 eV under  $n$ -type conditions (calculated as the difference between the sum of the formation energies of  $\text{Sn}_{\text{i}}^{2+}$  and  $V_{\text{Ga}}^{3-}$  and the formation energy of  $\text{Sn}_{\text{Ga}}^{+}$ ). In the kick-out mechanism, the reaction  $\text{Ga}_{\text{i}} + \text{Sn}_{\text{Ga}} \rightarrow \text{Sn}_{\text{i}}$  leads to a modest 0.46 eV increase in energy under  $n$ -type

conditions, but the  $\text{Ga}_{\text{i}}$  supplying the kick-out has a high formation energy, and must additionally overcome the repulsive Coulomb interaction with  $\text{Sn}_{\text{Ga}}^{+}$ . The vacancy mechanism is expected to have a far lower activation energy due to the low formation energy of  $V_{\text{Ga}}^{3-}$ ,

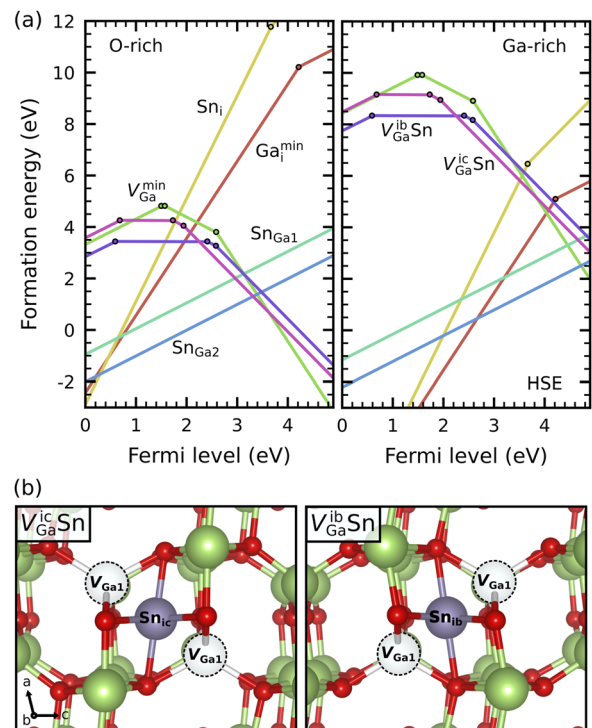


**FIG. 2.** Top: formation energy of  $\text{Ga}_{\text{i}}^{\text{min}}$ ,  $V_{\text{Ga}}^{\text{min}}$  (minimum formation energy over all considered  $\text{Ga}_{\text{i}}$  and  $V_{\text{Ga}}$  configurations),  $\text{Sn}_{\text{i}}$ ,  $\text{Sn}_{\text{Ga}1}$ ,  $\text{Sn}_{\text{Ga}2}$ ,  $V_{\text{Ga}}^{\text{ib}}\text{Sn}$ , and  $V_{\text{Ga}}^{\text{ic}}\text{Sn}$  under O-rich (left) and Ga-rich (right) conditions. Bottom: relaxed structures showing the  $V_{\text{Ga}}^{\text{ib}}\text{Sn}$  and  $V_{\text{Ga}}^{\text{ic}}\text{Sn}$  configurations.

$$E^f(V_{\text{Ga}}^{3-}) = 16.67 \text{ eV} + \Delta\mu_{\text{Ga}} - 3E_{\text{F}}, \quad (2)$$

where  $\Delta\mu_{\text{Ga}}$  can vary from 0 eV (Ga-rich) to  $\frac{1}{2}\Delta H_f(\beta\text{-Ga}_2\text{O}_3) = -5.11 \text{ eV}$  (O-rich). Here, it should be pointed out that a change from  $\text{O}_2$  to  $\text{N}_2$  annealing ambient will result in less O-rich conditions, which will increase the chemical potential of Ga and, thus, the formation energy of  $V_{\text{Ga}}^{3-}$ . This will suppress the diffusion of Sn in the vacancy mechanism, in line with the observation in Ref. 15. In addition to the low formation energy of  $V_{\text{Ga}}^{3-}$ , the formation of  $V_{\text{Ga}}\text{Sn}_{\text{Ga}}$  complexes will be favorable due to the attractive interaction between the  $\text{Sn}_{\text{Ga}}^+$  donor and  $V_{\text{Ga}}^{3-}$  acceptor, as shown in Sec. III B. The activation energy for diffusion is given by the formation energy of  $V_{\text{Ga}}$  reduced by the binding energy of the  $V_{\text{Ga}}\text{Sn}_{\text{Ga}}$  complex, plus the migration barrier of the complex,<sup>42</sup> i.e.,

$$Q = [E^f(V_{\text{Ga}}^q) - E_b(V_{\text{Ga}}\text{Sn}_{\text{Ga}})] + E_m(V_{\text{Ga}}\text{Sn}_{\text{Ga}}). \quad (3)$$

Note that this activation energy assumes diffusion of already formed  $\text{Sn}_{\text{Ga}}$  donors.  $V_{\text{Ga}}\text{Sn}_{\text{Ga}}$  binding energies and migration barriers obtained from hybrid functional calculations are presented in Secs. III B and III C. From the calculated activation energies, we conclude that the  $V_{\text{Ga}}$  mechanism will prevail over the interstitial–substitutional mechanisms in the relevant Fermi-level range. We note, however, that interstitial–substitutional mechanisms might play a role in out-of-equilibrium scenarios, e.g., when  $\text{Ga}_i$  are formed by ion implantation.

### B. $V_{\text{Ga}}\text{Sn}_{\text{Ga}}$ complex configurations and stability

The  $V_{\text{Ga}}\text{Sn}_{\text{Ga}}$  complex can potentially occur in many crystallographically inequivalent configurations. The relative energetics of 31 different  $V_{\text{Ga}}\text{Sn}_{\text{Ga}}$  configurations are provided and discussed in detail in the [supplementary material](#).<sup>37</sup> Below, we discuss trends in the relative stability of the different configurations and present the binding energy of the most favorable configuration.

As mentioned, the Ga vacancy in  $\beta\text{-Ga}_2\text{O}_3$  prefers to form split configurations, in which  $V_{\text{Ga}}$  is shared between two Ga sites with one  $\text{Ga}_i$  residing between them. Such a split vacancy could form next to a Sn substituting for Ga or with Sn as the interstitial in the split vacancy. Under  $n$ -type conditions,  $V_{\text{Ga}}^{\text{ic}}$  is the most favorable configuration of the isolated  $V_{\text{Ga}}$ , followed by  $V_{\text{Ga}}^{\text{ib}}$ .<sup>25</sup> Figure 2 shows the relaxed structures of the corresponding split vacancies with Sn replacing the Ga in the interstitial site, labeled here as  $V_{\text{Ga}}^{\text{ic}}\text{Sn}$  and  $V_{\text{Ga}}^{\text{ib}}\text{Sn}$ . The former is found to be the preferred configuration of the complex under  $n$ -type conditions, similar to the isolated  $V_{\text{Ga}}^{\text{ic}}$ .

Sn strongly prefers to substitute on the octahedral  $\text{Ga}_2$  site over the tetrahedral  $\text{Ga}_1$  site. The relative energetics of different  $V_{\text{Ga}}\text{Sn}_{\text{Ga}}$  configurations also correlate with the coordination environment of Sn in the complex. Configurations involving octahedral  $\text{Sn}_{\text{Ga}_2}$  are generally lower in energy than those involving tetrahedral  $\text{Sn}_{\text{Ga}_1}$ . The  $V_{\text{Ga}}^{\text{ib}}\text{Sn}$  and  $V_{\text{Ga}}^{\text{ic}}\text{Sn}$  configurations described above are also favorable in this regard, as the Sn atoms reside in the octahedral  $ib$  and  $ic$  sites. Among the less favorable configurations involving tetrahedral  $\text{Sn}_{\text{Ga}_1}$ , some are even unstable and will readily transform into other configurations, as explained in the [supplementary material](#).<sup>37</sup>

The binding energy of the  $V_{\text{Ga}}\text{Sn}_{\text{Ga}}$  complex can be calculated as the difference in formation energy between the complex and the sum of the formation energies of the isolated constituents ( $\text{Sn}_{\text{Ga}}$  and

$V_{\text{Ga}}$ ). For Fermi-level positions in the upper half of the bandgap, the lowest energy  $V_{\text{Ga}}^{\text{ic}}\text{Sn}$  configuration has a well-defined binding energy of 1.63 eV. If the Fermi level is lowered further,  $V_{\text{Ga}}$  will trap holes and lower its charge state, decreasing the Coulomb attraction and  $V_{\text{Ga}}\text{Sn}_{\text{Ga}}$  binding energy. By comparison,  $\text{Sn}_{\text{Ga}}$  forming complexes with other acceptors such as  $\text{Fe}_{\text{Ga}}$  have much lower binding energies (on the order of 0.4 eV for neutral complexes) and are not expected to significantly influence our conclusions.

### C. $V_{\text{Ga}}\text{Sn}_{\text{Ga}}$ complex migration barriers

As illustrated in Fig. 3, Ga vacancy-mediated diffusion of Sn involves three basic processes:<sup>43</sup> (i) exchange, where the Sn in the  $V_{\text{Ga}}\text{Sn}_{\text{Ga}}$  complex jumps into the  $V_{\text{Ga}}$ . This is the only process that changes the location of the impurity, but it is not sufficient on its own. (ii) Rotation, where a Ga atom that is immediately adjacent to the Sn atom jumps into the  $V_{\text{Ga}}$ , leaving the complex in a different configuration/orientation. (iii) Dissociation, where a different Ga atom jumps into the  $V_{\text{Ga}}$  and the complex is partially dissociated. Due to the large binding energy of the  $V_{\text{Ga}}\text{Sn}_{\text{Ga}}$  complex, process (iii) will likely occur at significantly lower rates than processes (i) and (ii). Thus, Sn migration will primarily proceed through a combination of exchange and rotation jumps.

$V_{\text{Ga}}\text{Sn}_{\text{Ga}}$  migration barriers were calculated for 50 different exchange, rotation, and dissociation jumps in total. The lowest energy pathways for  $V_{\text{Ga}}\text{Sn}_{\text{Ga}}$  migration in the three different crystal directions of  $\beta\text{-Ga}_2\text{O}_3$  were determined based on analysis of the resulting barriers. Starting from the lowest energy  $V_{\text{Ga}}^{\text{ic}}\text{Sn}$  configuration, we obtain similar migration barriers of 3.42, 3.15, and 3.37 eV for the [100], [010], and [001] directions, respectively, as listed in Table I. Note that these are overall migration barriers consisting of several individual jumps. Migration barriers from SCAN NEB calculations for all individual jumps of  $V_{\text{Ga}}\text{Sn}_{\text{Ga}}$  are listed in the [supplementary material](#),<sup>37</sup> along with a description of the migration pathways. Migration barriers based on a similar analysis for the isolated  $V_{\text{Ga}}$  from Ref. 39 are also included in Table I. The complex exhibits significantly higher overall migration barriers than  $V_{\text{Ga}}$ .

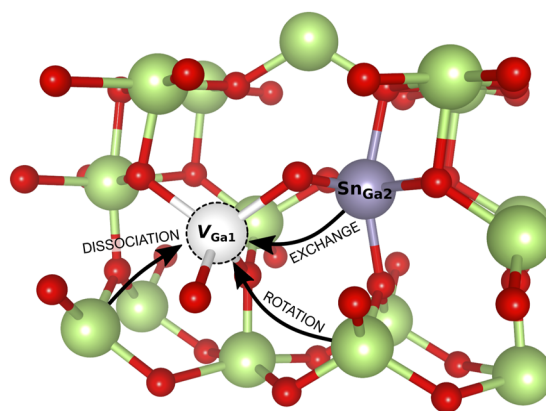


**FIG. 3.** Relaxed structure of the  $V_{\text{Ga}_1}\text{Sn}_{\text{Ga}_2}$  complex with arrows showing an exchange, rotation, and dissociation type jumps for the Sn migration process. The Ga, O, and Sn atoms are green, red, and purple, respectively, and the Ga vacancy is indicated by a white translucent circle with dashed outlines.

**TABLE I.** Binding energy ( $E_b$ ) of  $V_{Ga}^{3-}$  Sn, and overall migration barriers ( $E_m$ ) of  $V_{Ga}Sn_{Ga}$  and  $V_{Ga}$  for each crystal directions in  $\beta$ -Ga<sub>2</sub>O<sub>3</sub>, as obtained from hybrid functional calculations. The migration barriers of  $V_{Ga}$  are from Ref. 39.

	$E_m$ (eV)			$E_b$ (eV)
	[100]	[010]	[001]	
$V_{Ga}Sn_{Ga}$	3.42	3.15	3.37	1.63
$V_{Ga}$	2.08	2.08	0.97	...

This can be partially explained by the fact that Sn has to visit the unfavorable tetrahedral site during the migration process ( $Sn_{Ga1}$  is 1.06 eV higher in energy than  $Sn_{Ga2}$ ).<sup>37</sup> In addition, the low barrier of 0.97 eV for  $V_{Ga}$  migration along [001] is made possible by a three-split vacancy configuration,<sup>39</sup> which does not enable migration in the case of  $V_{Ga}Sn_{Ga}$ .

## D. Diffusion modeling

### 1. Reaction-diffusion model

The hybrid functional calculations strongly suggest a  $V_{Ga}$ -mediated diffusion process. To model the measured Sn concentration-depth profiles in Fig. 1(a) within this mechanism, we employ an RD model that involves a set of differential equations describing the relevant reactions between defects and their diffusion, as described in Refs. 44 and 45. This model has been employed previously to model the diffusion of Al,<sup>44,45</sup> Ga,<sup>46</sup> and In<sup>47</sup> donors in ZnO. See also Ref. 48 for a more general treatment of dopant diffusion in semiconductors on the basis of reaction-diffusion equations. The present model considers the formation and dissociation of mobile  $V_{Ga}Sn_{Ga}$  complexes under  $n$ -type conditions through the reaction  $V_{Ga}^{3-} + Sn_{Ga}^+ \rightleftharpoons (V_{Ga}Sn_{Ga})^{2-}$ . The time evolution of the  $V_{Ga}Sn_{Ga}$  complex concentration is described by Fickian diffusion,

$$\frac{\partial [V_{Ga}Sn_{Ga}]}{\partial t} = D_{V_{Ga}Sn_{Ga}} \frac{\partial^2 [V_{Ga}Sn_{Ga}]}{\partial x^2} - R_{V_{Ga}Sn_{Ga}}, \quad (4)$$

with a defect reaction term  $R_{V_{Ga}Sn_{Ga}}$  describing the time evolution of the  $Sn_{Ga}$  concentration, given by

$$R_{V_{Ga}Sn_{Ga}} = v[V_{Ga}Sn_{Ga}] - K[Sn_{Ga}][V_{Ga}]. \quad (5)$$

Here,  $D_{V_{Ga}Sn_{Ga}}$ ,  $v$ , and  $K$  are the diffusivity, dissociation rate, and formation rate of the  $V_{Ga}Sn_{Ga}$  complex, respectively. The formation rate is described by

$$K = 4\pi r D_{V_{Ga}}, \quad (6)$$

where  $D_{V_{Ga}}$  is the diffusivity of  $V_{Ga}$ , and  $r$  is the effective capture radius, which is estimated as the distance between the mobile  $V_{Ga}^{3-}$  acceptor and the  $Sn_{Ga}^+$  donor where the screened Coulomb potential energy equals the thermal energy  $k_B T$ .<sup>49,50</sup> This yields  $r$  values between 28 and 32 Å in the studied temperature range.

In the simulations, the initial  $[Sn_{Ga}]$  is determined from the measured profile for the preceding temperature step, and the net flux of  $V_{Ga}Sn_{Ga}$  complexes at the boundaries of the measured Sn concentration profiles is set to zero.

Considering the calculated migration barriers in Table I,  $V_{Ga}$  is anticipated to be highly mobile in the studied temperature interval.<sup>22,39</sup> Therefore, we assume an instantaneous establishment of the thermal-equilibrium concentration for  $V_{Ga}$ , which is controlled by the local Fermi-level position in the following manner:

$$[V_{Ga}] = N_s \exp\left(\frac{-E^f(V_{Ga}^{3-})}{k_B T}\right), \quad (7)$$

where  $N_s$  is the density of Ga sites in  $\beta$ -Ga<sub>2</sub>O<sub>3</sub> and  $k_B$  is the Boltzmann constant. The local Fermi-level position, which enters through the  $V_{Ga}$  formation energy [see Eq. (2)], can be approximated using the effective density of states at the conduction-band edge ( $N_c$ ) and the free electron concentration ( $n$ ),<sup>45,51</sup> resulting in

$$[V_{Ga}] = N_s \exp\left(-\frac{E_0^f(V_{Ga}^{3-}) - 3E_g(T)}{k_B T}\right) \left(\frac{n}{N_c}\right)^3, \quad (8)$$

where  $E_0^f(V_{Ga}^{3-})$  is the formation energy of  $V_{Ga}^{3-}$  when  $E_F$  is at the VBM, and  $E_g(T)$  is the bandgap at the simulated temperature.  $N_c$  is calculated using an electron effective mass value of 0.28  $m_e$ ,<sup>52</sup> and  $n$  is determined from the following charge-neutrality condition:

$$n = p + [Sn_{Ga}^+] - 3[V_{Ga}^{3-}] - 2[(V_{Ga}Sn_{Ga})^{2-}] + [N_d^+]. \quad (9)$$

The contribution of holes ( $p$ ) in the charge neutrality can be neglected under the relevant conditions.<sup>44</sup> In addition to Sn, SIMS measurements reveal the presence of Si and Fe as background impurities that can affect the free carrier concentration.  $Si_{Ga}$  is another shallow donor<sup>9</sup> and  $Fe_{Ga}$  acts as compensating acceptor under  $n$ -type conditions.<sup>53</sup> As discussed in Sec. III D 3, the low  $n$  in the epilayer region plays a crucial role in impeding the Sn diffusion, and the background impurities make an appreciable contribution to  $n$  in the epilayer. For this reason, we include an effective background-donor concentration ( $N_d^+$ ) of  $2 \times 10^{17}$  cm<sup>-3</sup> in the charge-neutrality condition, which is based on the measured concentrations of Si and Fe impurities in the epilayer region of the as-received sample, assuming that all impurities are Ga substitutional. This is indicated by the black dashed line in Fig. 1(b). In the substrate region,  $n$  will be mainly dictated by the high concentration of Sn donors.

### 2. Fitting parameters

The RD model contains the following fitting parameters:  $D_{V_{Ga}Sn_{Ga}}$ ,  $D_{V_{Ga}}$ ,  $v$ , and  $(E_0^f(V_{Ga}^{3-}) - 3E_g)$ . Several possible sets of values can provide the same quality of fits to the experimental data, i.e., a unique solution to Eqs. (4) and (5) does not exist. However, the parameters  $D_{V_{Ga}}$ ,  $v$ , and  $(E_0^f(V_{Ga}^{3-}) - 3E_g)$  can be fixed or constrained by using experimental data and the results from our hybrid functional calculations, as described below. A table listing the parameters used for the simulated profiles in Fig. 1 can be found in the [supplementary material](#).<sup>37</sup>

The narrowing of the bandgap from 4.9 eV as a function of increasing temperature is extrapolated from experimental measurements at temperatures from 22 up to 550 °C by Mock *et al.*<sup>54</sup> The resulting bandgap is between 4.11 and 3.95 eV in the studied temperature interval 1050–1250 °C. We note that the bandgap decreases with temperature scatters in the literature,<sup>54–57</sup> and its magnitude

has a strong influence on the value of  $E_0^f(V_{\text{Ga}}^{3-})$  used in the simulations. However, the  $E_0^f(V_{\text{Ga}}^{3-})$  value for other band gaps can always be obtained by referring back to Eq. (7); a change in  $E_g$  must be compensated by a threefold change in  $E_0^f(V_{\text{Ga}}^{3-})$  to maintain the exponential factor in Eq. (7) and, thus, the fits in Fig. 1.

$E_0^f(V_{\text{Ga}}^{3-})$  is treated as a fitting parameter in the simulations but is guided by the predicted formation energy in Eq. (2). We find that  $E_0^f(V_{\text{Ga}}^{3-})$  values decreasing from 12.8 to 12.4 eV as the temperature increases from 1050 to 1250 °C provide the best fits to the experimental data. The calculated formation energy in Eq. (2) depends on the chemical environment and is only valid for zero temperature. To enable an approximate comparison with the value used in the simulations, we use a tabulated value of  $\mu_{\text{O}}$  for equilibrium with 1 atm O<sub>2</sub> gas at 1150 °C<sup>58</sup> and assume no temperature and pressure dependence for bulk Ga and  $\beta$ -Ga<sub>2</sub>O<sub>3</sub>. Under these assumptions, a  $E_0^f(V_{\text{Ga}}^{3-})$  value of 14.0 eV can be estimated, which is reasonably close to the 12.7 eV used in the simulations, considering that the free-energy lowering due to vibrational entropy is not included in Eq. (2).

The  $V_{\text{Ga}}$  diffusivity, which enters the formation rate  $K$ , is given by  $D_{V_{\text{Ga}}} = D_0 \exp(-E_m(V_{\text{Ga}})/k_B T)$ . Here, the prefactor is set on the basis of an uncorrelated random walk, where it is approximately given by  $v_0 d^2$ . We use an average distance  $d$  of 3.3 Å for Ga jumps in  $\beta$ -Ga<sub>2</sub>O<sub>3</sub> and an attempt frequency  $v_0$  of  $1 \times 10^{14} \text{ s}^{-3}$  based on the reported Debye temperature of 738 K.<sup>59</sup> This results in a prefactor of  $1 \times 10^{-1} \text{ cm}^2 \text{ s}^{-1}$ . For the  $V_{\text{Ga}}$  migration barrier, we use the predicted value of 2.1 eV from Table 1, which is the barrier that must be surmounted to enable  $V_{\text{Ga}}$  migration in all three crystal directions. We note that setting  $E_m(V_{\text{Ga}})$  to the lower value of 1.0 eV predicted for the [001] direction has no effect on the simulated profiles, as discussed in Sec. III D 3.

The  $V_{\text{Ga}}\text{Sn}_{\text{Ga}}$  complex dissociation rate is described by  $\nu = \nu_0 \exp(-E_d(V_{\text{Ga}}\text{Sn}_{\text{Ga}})/k_B T)$ . Here, the dissociation energy  $E_d(V_{\text{Ga}}\text{Sn}_{\text{Ga}})$  is estimated as the sum of the calculated  $V_{\text{Ga}}$  migration barrier of 2.1 eV and  $V_{\text{Ga}}^{\text{ic}}\text{Sn}$  binding energy of 1.6 eV, resulting in 3.7 eV. In the formalism with an effective capture radius, the potential energy of the dissociated  $V_{\text{Ga}}^{3-}$  is slightly reduced by the amount of  $k_B T$ , which must be subtracted from  $E_d$ .<sup>46</sup>

### 3. Reaction-diffusion modeling results

Figure 1(a) shows the best fits to the experimental data obtained by using the fitting parameters described above and manually adjusting the complex diffusivity  $D_{V_{\text{Ga}}\text{Sn}_{\text{Ga}}}$ . The simulated Sn diffusion profiles exhibit close agreement with the experimental data for the whole range of studied temperatures.

Figure 4 shows an Arrhenius plot of the  $D_{V_{\text{Ga}}\text{Sn}_{\text{Ga}}}$  values extracted from the fitting. We obtain a diffusion coefficient of  $D_0 = 2 \times 10^{-1} \text{ cm}^2 \text{ s}^{-1}$ , which is close to the one used for  $V_{\text{Ga}}$ , and an activation energy of  $3.0 \pm 0.4 \text{ eV}$ . Within the RD model, this energy represents the migration barrier of the  $V_{\text{Ga}}\text{Sn}_{\text{Ga}}$  complex, as explained in Ref. 44. This migration barrier agrees well with the 3.37 eV barrier for  $V_{\text{Ga}}\text{Sn}_{\text{Ga}}$  migration along [001] obtained from NEB calculations. Here, it should be pointed out again that the model contains several fitting parameters that are fixed ( $V_{\text{Ga}}$  migration barrier and  $V_{\text{Ga}}\text{Sn}_{\text{Ga}}$  binding energy) or guided ( $V_{\text{Ga}}$  formation energy) by the hybrid functional calculations, which will influence the solution. However, the good agreement found between the

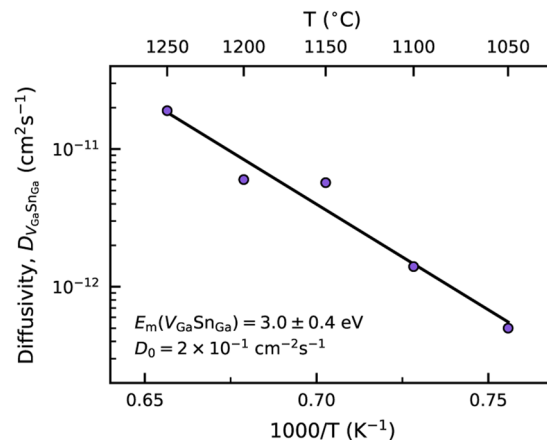


FIG. 4.  $V_{\text{Ga}}\text{Sn}_{\text{Ga}}$  complex diffusivities used to obtain the simulated Sn diffusion profiles shown in Fig. 1 as a function of the inverse absolute temperature. The activation energy and prefactor obtained from the linear fit are indicated.

predicted and extracted  $V_{\text{Ga}}\text{Sn}_{\text{Ga}}$  migration barrier is encouraging, i.e., the extracted results are consistent with the first-principles input.

The boxlike appearance of the measured Sn diffusion profiles can be understood from Fig. 1(b), showing the depth distribution of Sn,  $\text{Sn}_{\text{Ga}}$ ,  $V_{\text{Ga}}$ ,  $V_{\text{Ga}}\text{Sn}_{\text{Ga}}$ , and  $n$  resulting from RD modeling for the 1250 °C profile. The high Fermi-level position (high  $n$ ) in the Sn-doped substrate results in low formation energies and high concentrations of  $V_{\text{Ga}}$  and  $V_{\text{Ga}}\text{Sn}_{\text{Ga}}$ . At the diffusion front, the drop in  $\text{Sn}_{\text{Ga}}$  concentration and Fermi-level position (lower  $n$ ) results in a steep increase in the formation energy of  $V_{\text{Ga}}^{3-}$  because of its triple negative charge state. The resulting lower concentration of  $V_{\text{Ga}}$  and  $V_{\text{Ga}}\text{Sn}_{\text{Ga}}$  drastically impedes the migration of Sn and provides a sharp gradient in its concentration.<sup>45</sup> As  $V_{\text{Ga}}\text{Sn}_{\text{Ga}}$  complexes migrate to and dissociate at the diffusion front, the Fermi-level position is gradually raised by the transported  $\text{Sn}_{\text{Ga}}$  donors, and the front moves further into the epilayer.

In state-of-the-art  $\beta$ -Ga<sub>2</sub>O<sub>3</sub> grown by metalorganic chemical vapor deposition, the room-temperature free carrier concentration can be as low as  $\sim 10^{14} \text{ cm}^{-3}$ .<sup>2</sup> For Sn diffusion from a doped substrate or implanted layer into such material, we expect that the effective Sn diffusivity will be further suppressed with even steeper drops in concentration at the diffusion front (due to the strong dependence of  $[V_{\text{Ga}}]$  on the Fermi level). To illustrate this, Fig. 5 shows two simulated profiles for a 30-min anneal at 1250 °C, starting from the measured SIMS profile at 1200 °C. One profile was calculated using an effective background-donor concentration of  $2 \times 10^{17} \text{ cm}^{-3}$  and the other with a background-donor concentration of  $1 \times 10^{14} \text{ cm}^{-3}$ , in both cases keeping all other parameters fixed to those used for the simulations in Fig. 1. The lower background-donor concentration clearly leads to a slower advance of the diffusion front and a steeper decrease in concentration. This is in line with previous observations on Al diffusion in ZnO samples with different effective background-donor concentrations,<sup>45</sup> although the effect is weaker in ZnO due to the 2—rather than 3—charge state of  $V_{\text{Zn}}$ .

Finally, it may be instructive to discuss how some of the specific choices made for the fitting parameters  $D_{V_{\text{Ga}}}$  and  $\nu$  affect the

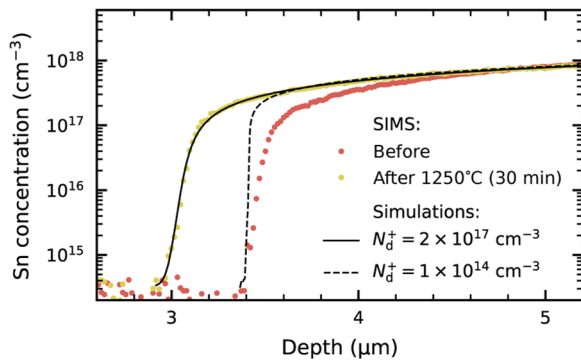


**FIG. 5.** Sn-concentration profiles before and after heat treatment for 30 min at 1250 °C measured by SIMS (dots) and Sn-concentration profiles after diffusion at 1250 °C (30 min) from the simulations using effective background-donor concentrations of  $2 \times 10^{17} \text{ cm}^{-3}$  (solid line) and  $1 \times 10^{14} \text{ cm}^{-3}$  (dashed line), keeping all other RD model parameters fixed.

RD modeling results. There is a strong coupling between different parameters in the model, with some affecting both the dissociation and formation rate of the  $V_{\text{Ga}}\text{Sn}_{\text{Ga}}$  complex.<sup>44</sup> For example, lowering the  $V_{\text{Ga}}$  migration barrier increases the formation rate, but the dissociation energy (estimated as the sum of the  $V_{\text{Ga}}$  migration barrier and  $V_{\text{Ga}}\text{Sn}_{\text{Ga}}$  binding energy) is then lowered by the same amount, leading to an increased dissociation rate. This is why we observe no difference in the profiles if  $E_{\text{m}}(V_{\text{Ga}})$  is decreased from 2.1 to 1.0 eV. Indeed, as shown in previous studies employing the RD model,<sup>45,46</sup> if the transport capacity of the vacancy is greater than that of the dopant–vacancy pair, the vacancy migration barrier will not be decisive. Similarly,  $v_0$  is inherent in both  $v$  and  $D_{V_{\text{Ga}}}$ . The binding energy of the  $V_{\text{Ga}}\text{Sn}_{\text{Ga}}$  complex, however, affects only the dissociation rate, so a change here must be compensated, e.g., by a change in  $E_0^f(V_{\text{Ga}}^{3-})$  to maintain the fits.

#### IV. CONCLUSION

In summary, we have studied the diffusion of Sn donors in  $\beta\text{-Ga}_2\text{O}_3$  by combining SIMS measurements with first-principles calculations. Sn diffusion from a Sn-doped bulk substrate into an epilayer is observed in the temperature interval 1050–1250 °C. Calculated formation energies of Sn-related and intrinsic defects show that  $V_{\text{Ga}}$  is the dominant vehicle for the Sn diffusion, where  $\text{Sn}_{\text{Ga}}$  migrates through the formation of an intermittent mobile  $V_{\text{Ga}}\text{Sn}_{\text{Ga}}$  complex. The activation energy for diffusion within this mechanism includes the formation energy of  $V_{\text{Ga}}$  in the triple negative charge state and is thus highly sensitive to the Fermi-level position, giving rise to steep drops in Sn concentration between the highly Sn-doped region and unintentionally  $n$ -type doped region. The time evolution of the Sn diffusion profiles measured by SIMS can be well simulated by employing a reaction–diffusion model. A  $V_{\text{Ga}}\text{Sn}_{\text{Ga}}$  migration barrier along [001] of  $3.0 \pm 0.4$  eV is extracted from the simulations, which is close to the 3.37 eV predicted from NEB calculations.

#### SUPPLEMENTARY MATERIAL

See the [supplementary material](#) for relative formation energies of different  $V_{\text{Ga}}\text{Sn}_{\text{Ga}}$  configurations, more details on the

migration barriers and pathways, and parameters used in the reaction–diffusion model.

#### ACKNOWLEDGMENTS

Financial support was acknowledged by the Research Council of Norway through the GO-POW project (Grant No. 314017) and the Air Force Office of Scientific Research (Grant No. FA9550-22-1-0165). The computations were performed on resources provided by UNINETT Sigma2—the National Infrastructure for High Performance Computing and Data Storage in Norway. This work used Stampede2 at Texas Advanced Computing Center (TACC) through Allocation No. DMR070069 from the Extreme Science and Engineering Discovery Environment (XSEDE), supported by the National Science Foundation (Grant No. ACI-1548562). This work was partially performed under the auspices of the U.S. DOE by Lawrence Livermore National Laboratory (LLNL) under Contract No. DE-AC52-07NA27344 and partially supported by LLNL Laboratory Directed Research and Development funding under Project No. 22-SI-003 and by the Critical Materials Institute, an Energy Innovation Hub funded by the U.S. DOE, Office of Energy Efficiency and Renewable Energy, Advanced Manufacturing Office.

#### AUTHOR DECLARATIONS

##### Conflict of Interest

The authors have no conflicts to disclose.

##### Author Contributions

**Ymir K. Frodason:** Conceptualization (equal); Data curation (equal); Formal analysis (equal); Funding acquisition (equal); Investigation (equal); Methodology (equal); Project administration (equal); Visualization (equal); Writing – original draft (equal); Writing – review & editing (equal). **Patryk P. Krzyzaniak:** Conceptualization (equal); Data curation (equal); Formal analysis (equal); Investigation (equal); Methodology (equal). **Lasse Vines:** Conceptualization (equal); Data curation (equal); Formal analysis (equal); Funding acquisition (equal); Investigation (equal); Methodology (equal); Project administration (equal); Supervision (equal); Writing – review & editing (equal). **Joel B. Varley:** Data curation (equal); Formal analysis (equal); Investigation (equal); Methodology (equal); Validation (equal); Writing – review & editing (equal). **Chris G. Van de Walle:** Formal analysis (equal); Investigation (equal); Methodology (equal); Supervision (equal); Validation (equal); Writing – review & editing (equal). **Klaus Magnus H. Johansen:** Conceptualization (equal); Data curation (equal); Formal analysis (equal); Funding acquisition (lead); Investigation (equal); Methodology (equal); Project administration (lead); Supervision (equal); Writing – review & editing (equal).

#### DATA AVAILABILITY

The data that support the findings of this study are available from the corresponding author upon reasonable request.

#### REFERENCES

- 1C. Janowitz, V. Scherer, M. Mohamed, A. Krapf, H. Dwell, R. Manzke, Z. Galazka, R. Uecker, K. Irmscher, R. Fornari, M. Michling, D. Schmeißer, J. R. Weber, J. B. Varley, and C. G. Van de Walle, *New J. Phys.* **13**, 085014 (2011).



- <sup>2</sup>F. Alema, Y. Zhang, A. Osinsky, N. Orishchin, N. Valente, A. Mauze, and J. S. Speck, *APL Mater.* **8**, 021110 (2020).
- <sup>3</sup>E. G. Villora, K. Shimamura, Y. Yoshikawa, K. Aoki, and N. Ichinose, *J. Cryst. Growth* **270**, 420 (2004).
- <sup>4</sup>H. Aida, K. Nishiguchi, H. Takeda, N. Aota, K. Sunakawa, and Y. Yaguchi, *Jpn. J. Appl. Phys.* **47**, 8506 (2008).
- <sup>5</sup>M. Higashiwaki, K. Sasaki, A. Kuramata, T. Masui, and S. Yamakoshi, *Appl. Phys. Lett.* **100**, 013504 (2012).
- <sup>6</sup>K. Sasaki, Q. T. Thieu, D. Wakimoto, Y. Koishikawa, A. Kuramata, and S. Yamakoshi, *Appl. Phys. Express* **10**, 124201 (2017).
- <sup>7</sup>K. Sasaki, M. Higashiwaki, A. Kuramata, T. Masui, and S. Yamakoshi, *IEEE Electron Device Lett.* **34**, 493 (2013).
- <sup>8</sup>P. M. Fahey, P. B. Griffin, and J. D. Plummer, *Rev. Mod. Phys.* **61**, 289 (1989).
- <sup>9</sup>J. B. Varley, J. R. Weber, A. Janotti, and C. G. Van de Walle, *Appl. Phys. Lett.* **97**, 142106 (2010).
- <sup>10</sup>M. J. Tadjer, J. L. Lyons, N. Nepal, J. A. Freitas, A. D. Koehler, and G. M. Foster, *ECS J. Solid State Sci. Technol.* **8**, Q3187 (2019).
- <sup>11</sup>Z. Galazka, *Semicond. Sci. Technol.* **33**, 113001 (2018).
- <sup>12</sup>S.-d. Lee, K. Kaneko, and S. Fujita, *Jpn. J. Appl. Phys.* **55**, 1202B8 (2016).
- <sup>13</sup>S. Rafique, L. Han, A. T. Neal, S. Mou, M. J. Tadjer, R. H. French, and H. Zhao, *Appl. Phys. Lett.* **109**, 132103 (2016).
- <sup>14</sup>M. J. Tadjer, C. Fares, N. A. Mahadik, J. A. Freitas, D. Smith, R. Sharma, M. E. Law, F. Ren, S. J. Pearton, and A. Kuramata, *ECS J. Solid State Sci. Technol.* **8**, Q3133 (2019).
- <sup>15</sup>R. Sharma, M. E. Law, M. Xian, M. Tadjer, E. A. Anber, D. Foley, A. C. Lang, J. L. Hart, J. Nathaniel, M. L. Taheri, F. Ren, S. J. Pearton, and A. Kuramata, *J. Vac. Sci. Technol.* **37**, 051204 (2019).
- <sup>16</sup>R. Sharma, M. E. Law, F. Ren, A. Y. Polyakov, and S. J. Pearton, *J. Vac. Sci. Technol.* **39**, 060801 (2021).
- <sup>17</sup>K. Sasaki, M. Higashiwaki, A. Kuramata, T. Masui, and S. Yamakoshi, *Appl. Phys. Express* **6**, 086502 (2013).
- <sup>18</sup>M. H. Wong, C.-H. Lin, A. Kuramata, S. Yamakoshi, H. Murakami, Y. Kumagai, and M. Higashiwaki, *Appl. Phys. Lett.* **113**, 102103 (2018).
- <sup>19</sup>R. Sharma, M. E. Law, C. Fares, M. Tadjer, F. Ren, A. Kuramata, and S. J. Pearton, *AIP Adv.* **9**, 085111 (2019).
- <sup>20</sup>V. M. Reinertsen, P. M. Weiser, Y. K. Frodason, M. E. Bathen, L. Vines, and K. M. Johansen, *Appl. Phys. Lett.* **117**, 232106 (2020).
- <sup>21</sup>Y. K. Frodason, C. Zimmermann, E. F. Verhoeven, P. M. Weiser, L. Vines, and J. B. Varley, *Phys. Rev. Mater.* **5**, 025402 (2021).
- <sup>22</sup>A. Kyrtsos, M. Matsubara, and E. Bellotti, *Phys. Rev. B* **95**, 245202 (2017).
- <sup>23</sup>J. B. Varley, H. Peelaers, A. Janotti, and C. G. Van de Walle, *J. Phys. Condens. Matter* **23**, 334212 (2011).
- <sup>24</sup>J. M. Johnson, Z. Chen, J. B. Varley, C. M. Jackson, E. Farzana, Z. Zhang, A. R. Arehart, H.-L. Huang, A. Genc, S. A. Ringel, C. G. Van de Walle, D. A. Muller, and J. Hwang, *Phys. Rev. X* **9**, 041027 (2019).
- <sup>25</sup>M. E. Ingebrigtsen, A. Y. Kuznetsov, B. G. Svensson, G. Alfieri, A. Mihaila, U. Badstübner, A. Perron, L. Vines, and J. B. Varley, *APL Mater.* **7**, 022510 (2019).
- <sup>26</sup>H. Peelaers, J. L. Lyons, J. B. Varley, and C. G. Van de Walle, *APL Mater.* **7**, 022519 (2019).
- <sup>27</sup>G. Henkelman, B. P. Uberuaga, and H. Jónsson, *J. Chem. Phys.* **113**, 9901 (2000).
- <sup>28</sup>PDE Solutions Inc, FLEXPDE.
- <sup>29</sup>P. E. Blöchl, *Phys. Rev. B* **50**, 17953 (1994).
- <sup>30</sup>G. Kresse and D. Joubert, *Phys. Rev. B* **59**, 1758 (1999).
- <sup>31</sup>A. V. Krukau, O. A. Vydrov, A. F. Izmaylov, and G. E. Scuseria, *J. Chem. Phys.* **125**, 224106 (2006).
- <sup>32</sup>G. Kresse and J. Furthmüller, *Phys. Rev. B* **54**, 11169 (1996).
- <sup>33</sup>C. Freysoldt, B. Grabowski, T. Hickel, J. Neugebauer, G. Kresse, A. Janotti, and C. G. Van de Walle, *Rev. Mod. Phys.* **86**, 253 (2014).
- <sup>34</sup>C. Freysoldt, J. Neugebauer, and C. G. Van de Walle, *Phys. Rev. Lett.* **102**, 016402 (2009).
- <sup>35</sup>Y. Kumagai and F. Oba, *Phys. Rev. B* **89**, 195205 (2014).
- <sup>36</sup>J. Sun, A. Ruzsinszky, and J. Perdew, *Phys. Rev. Lett.* **115**, 036402 (2015).
- <sup>37</sup>See [supplementary material](#) at [url] for relative formation energies of different  $V_{\text{Ga}}\text{Sn}_{\text{Ga}}$  configurations, more details on the migration barriers and pathways, and parameters used in the reaction-diffusion model.
- <sup>38</sup>J. B. Varley, "First-principles calculations 2," in *Gallium Oxide: Materials Properties, Crystal Growth, and Devices*, edited by M. Higashiwaki and S. Fujita (Springer International Publishing, Cham, 2020), pp. 329–348.
- <sup>39</sup>Y. K. Frodason, J. B. Varley, K. M. H. Johansen, L. Vines, and C. G. Van de Walle, *Phys. Rev. B* **107**, 024109 (2023).
- <sup>40</sup>S. J. Pearton, J. Yang, P. H. Cary, F. Ren, J. Kim, M. J. Tadjer, and M. A. Mastro, *Appl. Phys. Rev.* **5**, 011301 (2018).
- <sup>41</sup>C. Zimmermann, V. Rønning, Y. Kalmann Frodason, V. Bobal, L. Vines, and J. B. Varley, *Phys. Rev. Mater.* **4**, 074605 (2020).
- <sup>42</sup>H. Mehrer, *Diffusion in Solids: Fundamentals, Methods, Materials, Diffusion-Controlled Processes*, Springer Series in Solid-State Sciences (Springer, Berlin, Heidelberg, 2007).
- <sup>43</sup>D. Steiauf, J. L. Lyons, A. Janotti, and C. G. Van de Walle, *APL Mater.* **2**, 096101 (2014).
- <sup>44</sup>K. M. Johansen, L. Vines, T. S. Bjørheim, R. Schifano, and B. G. Svensson, *Phys. Rev. Appl.* **3**, 024003 (2015).
- <sup>45</sup>T. N. Sky, K. M. Johansen, V. Venkatachalapathy, B. G. Svensson, L. Vines, and F. Tuomisto, *Phys. Rev. B* **98**, 245204 (2018).
- <sup>46</sup>T. N. Sky, K. M. Johansen, H. N. Riise, B. G. Svensson, and L. Vines, *J. Appl. Phys.* **123**, 055701 (2018).
- <sup>47</sup>T. N. Sky, K. M. Johansen, Y. K. Frodason, T. Aarholt, H. N. Riise, Ø. Prytz, B. G. Svensson, and L. Vines, *Semicond. Sci. Technol.* **34**, 025011 (2019).
- <sup>48</sup>H. Bracht, *Phys. Rev. B* **75**, 035210 (2007).
- <sup>49</sup>T. R. Waite, *J. Chem. Phys.* **28**, 103 (1958).
- <sup>50</sup>M. S. Janson, A. Hallén, M. K. Linnarsson, and B. G. Svensson, *Phys. Rev. B* **64**, 195202 (2001).
- <sup>51</sup>K. M. Johansen, J. S. Christensen, E. V. Monakhov, A. Y. Kuznetsov, and B. G. Svensson, *Appl. Phys. Lett.* **93**, 152109 (2008).
- <sup>52</sup>M. Mohamed, C. Janowitz, I. Unger, R. Manzke, Z. Galazka, R. Uecker, R. Fornari, J. R. Weber, J. B. Varley, and C. G. Van de Walle, *Appl. Phys. Lett.* **97**, 211903 (2010).
- <sup>53</sup>M. E. Ingebrigtsen, J. B. Varley, A. Y. Kuznetsov, B. G. Svensson, G. Alfieri, A. Mihaila, U. Badstübner, and L. Vines, *Appl. Phys. Lett.* **112**, 042104 (2018).
- <sup>54</sup>A. Mock, J. VanDerslice, R. Korlacki, J. A. Woollam, and M. Schubert, *Appl. Phys. Lett.* **112**, 041905 (2018).
- <sup>55</sup>T. Onuma, S. Saito, K. Sasaki, K. Goto, T. Masui, T. Yamaguchi, T. Honda, A. Kuramata, and M. Higashiwaki, *Appl. Phys. Lett.* **108**, 101904 (2016).
- <sup>56</sup>C. Sturm, R. Schmidt-Grund, V. Zviagin, and M. Grundmann, *Appl. Phys. Lett.* **111**, 082102 (2017).
- <sup>57</sup>L. Cheng, Y. Zhu, W. Wang, and W. Zheng, *J. Phys. Chem. Lett.* **13**, 3053 (2022).
- <sup>58</sup>K. Reuter and M. Scheffler, *Phys. Rev. B* **65**, 035406 (2001).
- <sup>59</sup>Z. Guo, A. Verma, X. Wu, F. Sun, A. Hickman, T. Masui, A. Kuramata, M. Higashiwaki, D. Jena, and T. Luo, *Appl. Phys. Lett.* **106**, 111909 (2015).